PERIODICO di MINERALOGIA
established in 1930

DIPARTIMENTO
DI SCIENZE DELLA TERRA
SAPIENZA
UNIVERSITÀ DI ROMA

An International Journal of
Mineralogy, Crystallography, Geochemistry,
Ore Deposits, Petrology, Volcanology
and applied topics on Environment, Archaeometry and Cultural Heritage

Mineralogy and origin of peralkaline granite-syenite nodules ejected in Pleistocene basalt from Bulhary, southern Slovakia

Monika Huraiová [a], Patrik Konečný [b], Ivan Holický [b], Stanislava Milovská [c], Ondrej Nemec [a], Vratislav Hurai [d,*]

[a] Department of Mineralogy and Petrology, Comenius University, 842 15 Bratislava, Slovakia
[b] State Geological Institute of Dionýz Štúr, 817 04 Bratislava, Slovakia
[c] Institute of Earth Sciences, Slovak Academy of Sciences, 840 05 Bratislava, Slovakia
[d] Institute of Earth Sciences, Slovak Academy of Sciences, 974 01 Banská Bystrica, Slovakia

ARTICLE INFO

Submitted: June 2016
Accepted: November 2016
Available on line: November 2016

* Corresponding author:
vratislav.hurai@savba.sk

DOI: 10.2451/2016PM651

How to cite this article:
Huraiová M. et al. (2017)
Period. Mineral. 86, 1-17

ABSTRACT

Peralkaline, Si-oversaturated, Al-depleted (sodium metasilicate-normative) granite xenoliths in Pleistocene alkali basalts of the Carpathian back-arc basin (Pannonian Basin) represent a new type of igneous rocks in Western Carpathians. Investigated granites contain skeletal K-feldspars associated with quartz, pyroxene, amphibole and fluorapatite. Neptunite-like mineral occurs together with quartz, amphibole, Na-Nb-REE-rich titanite and an unknown phosphate within hollows in skeletally grown K-feldspars. Interstitial amphiboles correspond to katophorite, richterite, obertiite and arfvedsonite. Amphiboles from hollows exhibit low analytical totals, high contents of alkalis (up to 11 wt% Na_2O+K_2O) combined with deficient C-site and excessive A-site cations. The analytical bias can be eliminated by the addition of 0.96-1.05 apfu Li, 1.67-1.73 wt% Li_2O), thus obtaining the amphibole stoichiometry corresponding to leakeite, albeit with increased Fe^{3+} and Mn^{3+} contents. Apatite compositions are aligned along the $5Ca^{2+}=3Sr^{2+}+Na^{+}+LREE^{3+}$ substitution trend characteristic for peralkaline rocks. Pyroxenes evolve from early diopside to late titanian aegirine, thus reflecting an increasing oxygen fugacity during magmatic differentiation. Strongly oxidizing conditions in final stages of the magmatic differentiation are reflected in up to 25 mol.% $KFe_3+Si_3O_8$ component in late K-feldspar, enrichment in high-valence C-site cations, particularly Fe^{3+} and Mn^{3+} in amphiboles, possible ferri-neptunite component $\square(M^{+})_2Li(Mn,Fe^{3+})_3TiSi_8O_{24}$ in "neptunite", and accessory hematite. The oxidized peralkaline granites are another member of the Tertiary intra-plate granitoid suite revealed in the northern promontory of the Pannonian Basin. The strong Al-depletion of the granites can be attributed to the accumulation of diopside in their mafic parental magma. A mantle-derived origin of granite xenoliths is indicated by blebby Cu-Ni-Co sulphides that usually originate from mafic magmas by liquation, but they also sporadically occur in intermediate-to-acidic alkalic residual melts after fractional crystallization and crystal accumulation from lamprophyric magma.

Keywords: neptunite; leakeite; hollow sanidine; peralkaline granite; alkali basalt; xenolith; Pannonian basin; Western Carpathians.

INTRODUCTION

Late-Miocene to Pleistocene alkali basalt volcanic centres extending over the northern margin of the Pannonian basin ejected fragments of exotic granitoids unknown from other neighbouring tectonic units. Orthopyroxene granites from Pinciná maar in western part of the volcanic field (Lučenec Basin) represented hitherto the only rock-type characterized using a set of complementary mineralogical, geochemical and geochronological methods (Huraiová et al., 1996, 2005;

Hurai et al., 2010). Detailed study of granite xenoliths from other volcanic centers has been hindered by small xenolith dimensions, only rarely exceeding several centimeters in diameter.

Here we report on a basaltic lava flow with granite xenoliths, whose compositions differ strongly from those described previously from the Pinciná maar. Electron probe micro-analytic and Raman spectroscopic study was conducted to characterize rock-forming minerals. Special emphasis was given to chemical and Raman spectrometric characterization of neptunite-like mineral, which may be analogous to rare accessory neptunite described from peralkaline rocks. Crystallization conditions, source and nature of parental magmas were constrained from compositions of major and minor rock-forming minerals, as well as silicate melt inclusions in diopside.

ANALYTICAL TECHNIQUES

Electron probe micro-analyses were conducted using a CAMECA SX-100 electron probe at the Geological Survey of Slovakia, Bratislava. The electron probe was calibrated using the following minerals, pure chemical compounds and elements: F-CaF_2, Cl-NaCl, Na-albite, Si-wollastonite/orthoclase, K-orthoclase, Ca-wollastonite/apatite, P-apatite, Fe-fayalite, Mn-rhodonite, Mg-forsterite, Sr-$SrTiO_3$, Ba and–barite, Pb-$PbCO_3$, Zn-willemite, Al-Al_2O_3, V-metallic vanadium, Cr-metallic chromium, Nb-columbite, Ti-TiO_2, Zr-$ZrSiO_4$, Y-YPO_4, REE-$REEPO_4$. Counts were measured at 15 kV accelerating voltage, 20 nA beam current, and 5 μm beam diameter. An extended beam diameter of 20 μm was applied to silicate glass to prevent loss of alkalis. Raw analyses were recalculated to weight percents of oxides using a PAP correction procedure (Pouchou and Pichoir, 1984).

Raman spectra were recorded using a LabRam HR800 spectrometer (Horiba Ltd., Japan) with 1800 grooves/mm (point analyses) and 600 grooves/mm (maps) gratings. Samples were illuminated with a 17 mW LHX1 CVI Melles Griot 632.8 nm He-Ne laser or a 300 mW Nd-YAG laser tuned at 532 nm. A long-working-distance LMPLanFI Olympus 100×0.8 objective of an Olympus BX-41 optical microscope focused the laser beam and collected the scattered light with a Peltier-cooled (-70 °C), multi-channel Synapse CCD detector, 1024×256 pixels) at spectral resolutions of 0.5 cm^{-1} (point analyses) or 1.7 cm^{-1} (maps). Point analyses were also obtained using the 532 and 638 nm excitations of a 18 mW Nd-YAG laser of an Xplora system (Horiba Ltd., Japan) coupled with an Olympus BX-51 microscope. Spectral resolution of the 20 cm spectrometer and the 1800 grooves/mm grating corresponded to 1.8 and 1.0 cm^{-1} for the two respective excitations.

GEOLOGICAL BACKGROUND

Granite-syenite nodules occur in basaltic lava flow exposed in the Bulhary open pit (48°17'19.34"N, 19°51'43.25"E), about 3.5 km NE of Fiľakovo town, southern Slovakia. The lava flow is a part of complex volcanic structure consisting of maar-diatreme infillings, cinder cones, lava flows and lacoliths. Radiometric K/Ar dating of the maar-related basaltic dyke yielded an age of 1.6±0.15 Ma, whereas the associated basaltic lava flow and related cinder cone were dated at 1.51±0.22 and 1.16±0.3 Ma, respectively (Konečný et al., 2003). The Bulhary maar together with its feeding channel is hosted in Lower Miocene sands and silts (Konečný and Lexa, 2003).

The Bulhary maar belongs to an intra-plate post-collision magmatic association genetically linked with the decompression melting of depleted asthenosphere (Downes et al., 1995; Dobosi et al., 1995; Konečný et al., 1995, 2002; Pécskay et al., 2006). The asthenosphere updoming and concomitant partial melting of the mantle was triggered by thermal subsidence and relaxation established after the Middle-Miocene, alpine-type subduction (Konečný et al., 2002; Seghedi et al., 2004). Volcanic activity in the study area occurred within the interval from 7 to 1 Ma (Konečný et al., 1995) and volcanic centres moved from north-western to south-eastern parts of the volcanic field.

PETROGRAPHY AND MINERALOGY

Granite nodules, 1-5 cm in diameter, contain bottle-green aegirine needles, up to 1 mm in length, embedded in white quartz-feldspar matrix. The nodules are wrapped in a 0.2-1 mm wide clinopyroxene-rich selvedge (Figure 1 a,b), which grades into the outermost syenitic shell.

Individual parts of xenoliths differ in terms of their contrasting silica saturation that results in specific mineral assemblages (Table 1). The central, silica-oversaturated granite part contains isometric, euhedral to subhedral, pale-green diopside-augite overgrown by bottle-green Ti-rich aegirine-augite. Typical spinifex-like texture (Figure 1c) is created by radial-concentric and feather-like aggregates of potassium feldspar, apatite and ocassionally also augite, which all postdate pyroxene phenocrysts (Figure 1 c,d). Intergranular matrix is filled with pale-blue, conchoidally fractured quartz. Some xenoliths (sample Bul8, Bul7) contain abundant brown interstitial amphibole, which postdates feldspar and apatite. In other xenolits (Bul2), the interstitial amphibole is lacking. Hematite is common accessory intergranular phase in all xenoliths. Chalcopyrite represents the latest phase occurring in interstitial spaces of quartz-feldspar matrix (Figure 1 e-g). Chalcopyrite aggregates contain inclusions of quartz, feldspar, aegirine and oval Ni-Co sulphide inclusions decorated by shrinkage cracks (Figure 1f). All

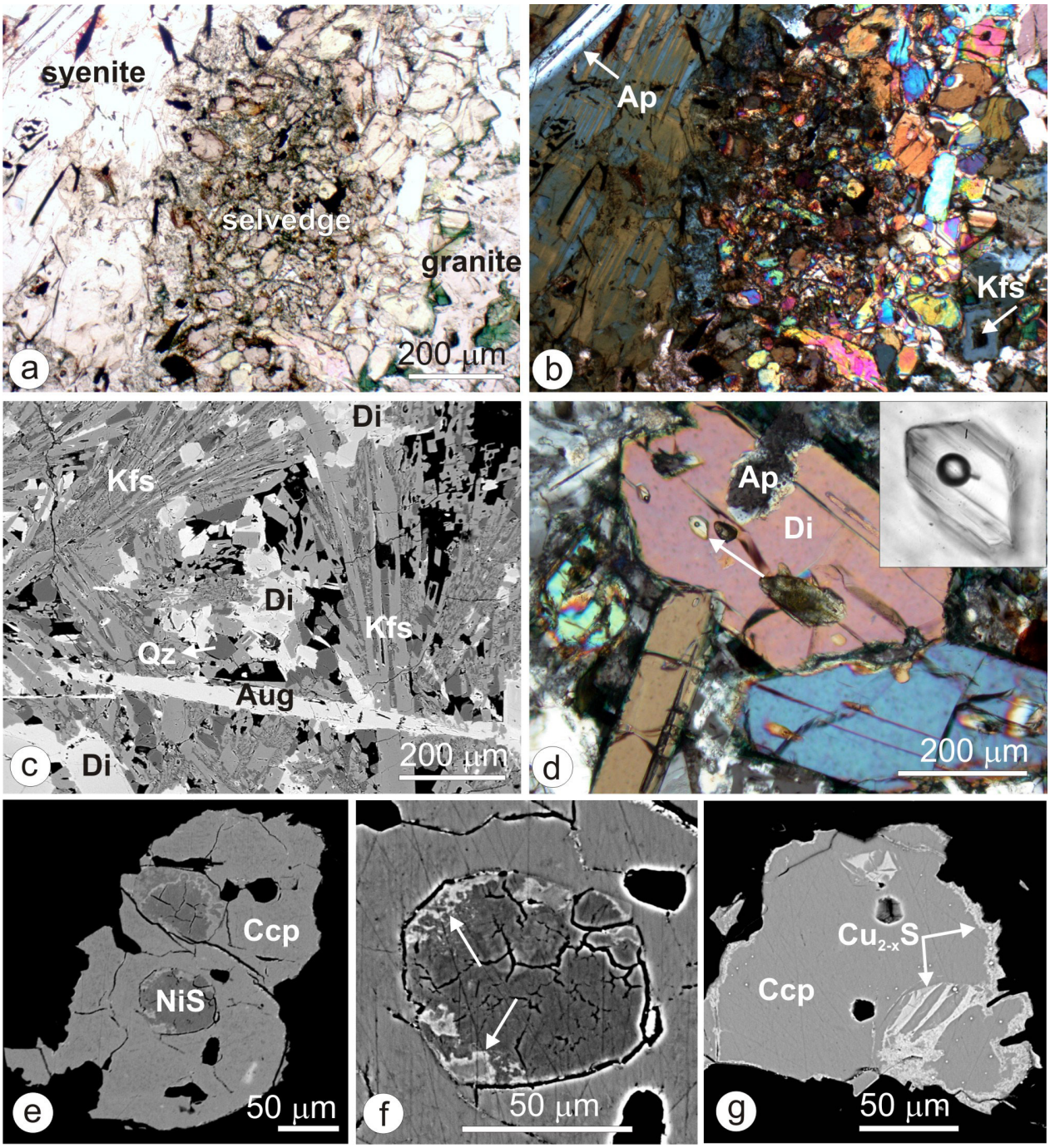

Figure 1. Photomicrographs of composite granite-syenite xenoliths. a) Diopside-rich selvedge dividing the syenitic envelope (left) from the granite core (right) with bottle-green aegirine. Opaque grains and laths in the syenite and the selvedge correspond to ilmenite and titanomagnetite. Transmitted plane-polarized light, sample Bul2. b) Previous image in crossed polarizers. Arrows indicate bladed apatite crystal (Ap) in plagioclase-feldspathoid matrix of the syenite part and skeletal potassium feldspar with central hollow (Kfs) in the granite part. c) Spinifex texture of granite core with elongated augite crystals (Aug), isometric diopside grains (Di) overgrown by bright aegirine, and skeletally grown radial aggregates of potassium feldspar (Kfs) cemented by quartz (Qz). Back-scattered electron (BSE) image, sample Bul2. d) Diopside phenocrysts with resorbed apatite (Ap) and silicate melt inclusion indicated by an arrow. Inset shows enlarged view of two-phase melt inclusion composed of vapour bubble and silicate glass. Plane-polarized transmitted light, sample Bul2. e) Chalcopyrite (Ccp) with two oval Ni-sulphide inclusions (NiS). Back-scattered electron image, sample Bul7. f) Enlarged view of the previous image showing contraction cracks in the Ni-rich inclusion and Cu-sulphide phases (arrows) grown along the inclusion-chalcopyrite phase boundary. g) View of interstitial chalcopyrite (Ccp) with bright Cu-rich sulphidic phases replacing the chalcopyrite along grain margins and cracks. Back-scattered electron image, sample Bul7.

Table 1. Mineral composition of composite granite-syenite xenoliths.

Rock	Granite	Syenite			
Mineral	Major	Minor	Accessory	Major	Minor
Amphibole	+				
Apatite	+			+	
K-feldspar	sanidine			+	
Feldspathoid				nepheline, sodalite	leucite
Quartz	+				
Fe-(Ti) oxide			hematite	ilmenite,	
titanomagnetite					
Sulphide			chalcopyrite, Ni-sulphide		
Mica					phlogopite
Olivine					forsterite
Plagioclase		anorthoclase		albite	
Pyroxene	diopside, aegirine	augite, aegirine-augite		Al-diopside	
Other			neptunite, titanite		

chalcopyrite grains are replaced along fractures and grain boundaries by Cu-rich sulphides (Figure 1g).

The marginal silica-undersaturated syenitic shell is dominated by alkali feldspars, feldspathoids (nepheline, sodalite, leucite), Fe-Ti oxides and apatite. Subordinate phases are represented by aluminian-titanian diopside, forsteritic olivine, phlogopite and interstitial silicate glass of trachytic composition. Qualitative modal composition of the outer envelope corresponds to a nepheline-sodalite syenite. Quartz, amphibole, aegirine-augite, aegirine and sulphides have not been recognized in the syenite part, whereas Fe-Ti oxides and phlogopite have been missing in the granite.

The diopside selvedge contains Fe-Ti-oxide grains and laths with exsolved Mg-rich ilmenite and Al-rich titanomagnetite that are chemically identical with those occurring in the syenite envelope. Also compositions of selvedge clinopyroxenes overlap those in the syenite. Hence, the selvedge obviously represents a cumulate formed along boundaries of the granite nodules.

Primary two-phase silicate glass-vapour inclusions occur in granite-hosted diopside phenocrysts (Figure 1d). The silicate glass is homogeneous, but small amphibole daughter crystals (<5 vol.%) occasionally occur in some inclusions. Chemical composition of the homogeneous glass corresponds to a peralkaline (NK/A=1.54, AI= -0.05), potassic, metaluminous (A/NKC=0.64) granite/ commendite (Table 2). The melt composition results in normative quartz, hypersthene and sodium metasilicate, thus emphasizing its silica-oversaturated and Al-deficient character. Raman spectroscopic analysis of the silicate glass did not reveal any detectable molecular water or hydroxyl groups.

Granite nodules comprise two types, which differ in terms of the amphibole abundance and the Fe-content in the potassium feldspar. One granite type (samples Bul5, Bul7, Bul8) contains abundant diopside postdated by ubiquitous amphibole, aegirine and K-feldspar with less than 1.7 wt% Fe_2O_3tot. Sample Bul2 is exceptional as it contains accessory amphibole crystallized only within hollows in skeletal K-feldspars with up to 8.5 wt% Fe_2O_3tot. In contrast to granite, K-feldspars of syenite shells are depleted in Fe_2O_3tot (always below 0.6 wt%), but they are locally enriched in BaO (up to 4.5 wt%).

Skeletal growth is a peculiar feature of granite xenoliths studied, particularly those devoid of intergranular amphiboles. Larger feldspar crystals contain an elongated central hollow oriented parallel with the c-crystallographic axis (Figure 2). Some hollows are empty, but many are filled with crystal aggregates of amphibole, neptunite-like mineral, aegirine, Na-Sr-REE-rich apatite, and Na-REE-Nb-rich titanite (Figure 3). The specific hollow assemblage is not replicated in the granite matrix except for some skeletal apatite crystals, grading from normal fluorapatite at margins towards the Na-Sr-REE-rich variety around the central hollow. Compositions of amphiboles from hollows also strongly differ from those of matrix amphiboles and significant compositional differences have also been recorded between "neptunites" in the two granite types.

Table 2. Chemical and normative compositions (wt%) of silicate glass inclusion in diopside from sample Bul2

Chemical composition		Normative composition	
SiO_2	74.66	K-feldspar	36.50
TiO_2	0.79	quartz	33.73
Al_2O_3	9.70	albite	15.27
$FeO_{tot.}$	3.71	hypersthene	7.39
MnO	< 0.07	Na_2SiO_3	5.84
MgO	0.22	rutile	0.60
CaO	0.13	titanite	0.46
Na_2O	4.99	halite	0.21
K_2O	6.20		
Cl	0.23		
F	< 0.11		

Feldspars

Compositions of feldspar aggregates correspond mostly to Na-sanidine and in a lesser extent to anorthoclase. Individual crystals are zoned: Fe_2O_3tot concentrations increase from ~1 wt% in margins up to 8.5 wt% in thin layers surrounding the central hollow. MgO contents are negligible (< 0.19 wt%). The low MgO contents and the negatively correlated Al and Fe atomic proportions indicate an Fe^{3+}-for-Al^{3+} substitution and up to 25 mol. % of the $KFe^{3+}Si_3O_8$ component (Table S1, Figure 4). Feldspars with increased Fe^{3+} contents also exhibit excess of Si cations over 3 apfu as well as a moderate cationic deficit below the ideal value of 5 apfu. The feldspar zoning is roughly correlated with the composition of the hollow assemblage: maximum iron contents occur around neptunite-filled hollows, whereas lower Fe_2O_3tot contents, around 4.5 wt%, have been encountered around amphibole-filled hollows.

Raman spectroscopic analysis was performed to corroborate the structural state of ferrian feldspars. Vibrational spectra recorded in cross-sections parallel with the c-axis of radial aggregates are characterized by two group I bands at 469 and 509 cm^{-1} attributed to ring-breathing modes of four-membered rings of tetrahedra (Figure 5). These bands are accompanied by wide group II and III bands at ~280 and 156 cm^{-1}, reflecting rotation-translation modes of the four-membered rings and cage-shears, respectively (Freeman et al., 2008). The low ordering degree of the investigated feldspars is corroborated by the lower intensity of the Ib band compared to that of the Ia band, by negligible Ic band at 454-460 cm^{-1}, broadening of the lattice vibration band at 280 cm^{-1}, and a generally smaller number of bands compared to those in ordered microcline and plagioclase (Makreski et al., 2009). The vibrational spectrum of ferrian feldspar from Bulhary is almost identical with that of the Na-sanidine megacryst from an alkali basalt from the same volcanic field, with structural characteristics of strongly disordered high-sanidine endmember as defined by Kroll and Ribbe (1983).

Pyroxenes

Crystallochemical formulae of pyroxenes were calculated using a WinPyrox computer program (Yavuz, 2013) accommodated to the approved IMA classification scheme (Morimoto et al., 1989). Maximum Fe^{3+} contents have been derived either according to Ryburn et al. (1976) or Papike et al. (1974).

Compositions of hollow pyroxenes correspond to aegirine (Table S2), whereas matrix pyroxenes range from diopside through aegirine-augite to aegirine. The hollow pyroxenes are significantly enriched in titanium compared to those in the matrix. Locally increased ZrO_2 and Nb_2O_5 contens, up to 0.6 and 0.5 wt%, respectively, have also been recorded in the hollow pyroxenes. Majority of Ti-rich pyroxenes from granite nodules cluster beyond the Q+J=2 line defining the boundary for "normal" pyroxenes, thus indicating the presence of a $NaR^{2+}_{0.5}Ti^{4+}_{0.5}Si_2O_6$ component (Figure 6).

Chemical analyses of granite pyroxenes create a trend almost parallel with the diopside-aegirine join (Figure 7) diagnostic of an increasing amount of ferric iron content during the magmatic differentiation. Almost all pyroxenes from hollows overlap the aegirine apex, thus reflecting the maximum Fe^{3+} concentration in the pyroxene structure. In contrast to granite, selvedge and syenite pyroxenes are aligned along the diopside-hedenbergite join, thus indicating the dominant ferrous iron during magmatic differentiation.

Apatites

Chemical analyses of apatites were recalculated to 26 (O,OH,F,Cl) anions as recommended by Pasero et al. (2010), and then normalised to an ideal apatite formula $A_{10}(TO_4)_6X_2$ by adjustment to 10 A-site anions (Table S3). Hydroxyl content was derived as 2-(Cl+F). The procedure fixes a total of 16 cations and the ratio of A- and T-site cations equivalent to 10:6 by assuming the hypothetical C content allocated in T-site (expressed as CO_3^{2-}) recalculated as C=6-P-Si-As-S (Seifert et al., 2000). Uncertainties in the inferred crystallochemical formulae may arise from the possible presence of an unknown O_2- content, substituting for monovalent cations in the X-site.

All investigated apatites corresponded to fluorapatite, with fluorine content ranging from 2.52 to 3.61 wt%, 1.39-1.92 apfu). OH/O contents were below 0.61 apfu and recalculated H_2O concentrations attained 0.52 wt%. Granite apatites have been locally enriched in SrO

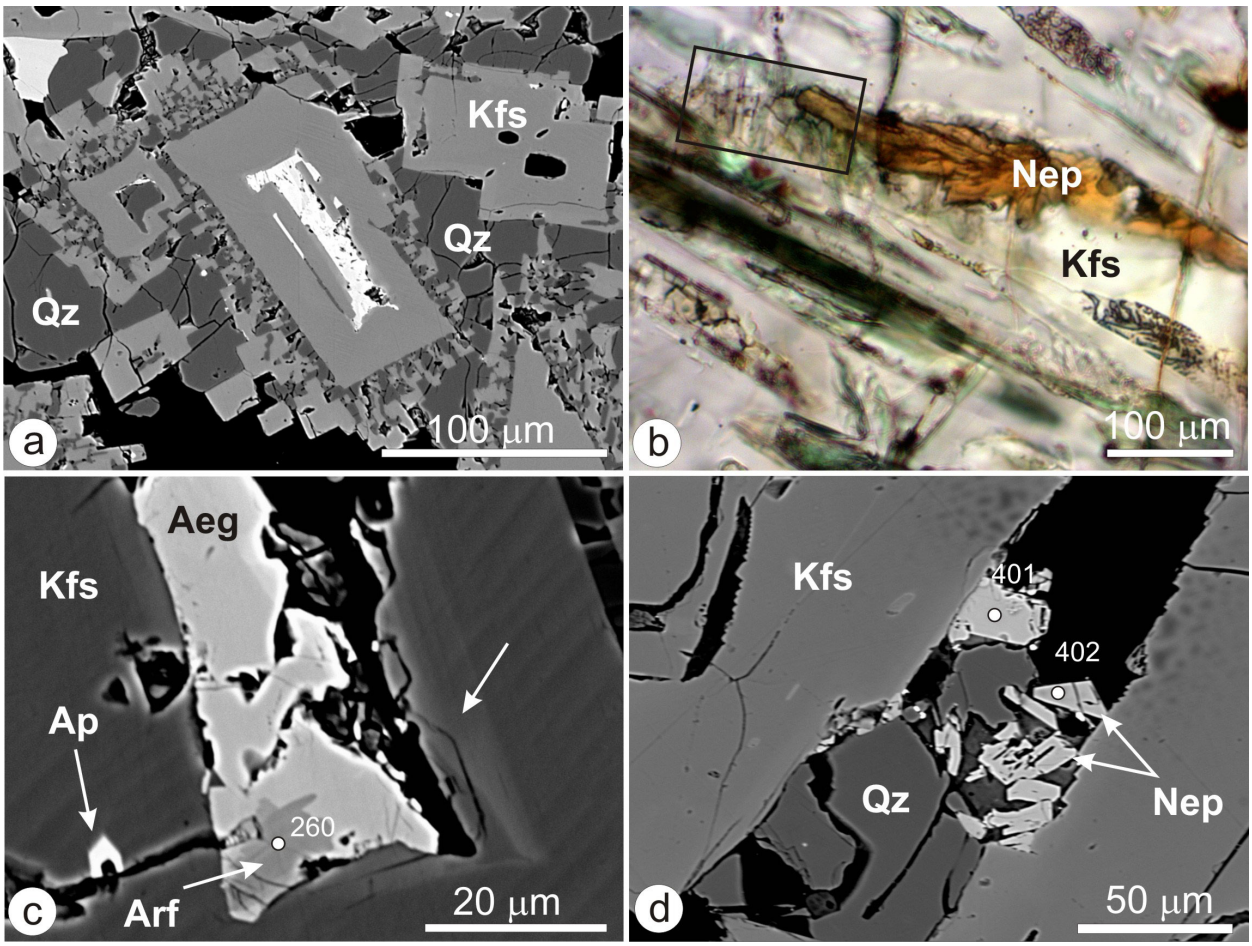

Figure 2. a) Fractal growth of ferrian potassium feldspar (Kfs) in quartz matrix (Qz). Larger feldspar crystals contain central cavity (hollow), which is either empty, or filled with quartz, drusy aggregates of neptunite-like mineral, amphibole+aegirine, or amphibole+"neptunite" intergrowths (bright area in the central crystal, see also Figure 3). BSE image, sample Bul2. b) Longitudinal view of central hollow in ferrian feldspar (Kfs) showing columnar orange-brown "neptunite" and unidentified transparent anhedral crystals. The black rectangle delineates the area selected for Raman mapping as displayed in Figure 11. Bottle-green minerals correspond to intergranular aegirine-augite. Transmitted plane-polarized light, sample Bul2. c) View of a hollow filled with aegirine (Aeg) and arfvedsonite (Arf). Euhedral apatite (Ap) grows along a crack in the feldspar host (Kfs). Bright arrow indicates Fe-rich zone containing up to 4 wt% Fe_2O_3 in the proximity of the central hollow. Sample Bul2. d) View of a hollow in low-iron K-feldspar filled with anhedral quartz (Qz) and subhedral "neptunite" (Nep). BSE image, sample Bul8. Numbered circles in c) and d) correspond to analytical points of electron probe micro-analyses.

(max. 7.75 wt%, 0.86 apfu Sr), Na_2O (max. 4.42 wt%, 1.68 apfu Na), and REE (max. 19.5 wt%, 1.49 apfu Y+REE). Systematic depletion in Ca accompanied by an enrichment in Sr, Na and REE have been recorded in matrix crystals, resorbed apatite inclusions in diopside as well as in apatites from hollows (Figure 8). This trend suggests a $5Ca^{2+}=3Sr^{2+}+Na^{+}+LREE^{3+}$ (apatite-belovite) substitution in the Ca-site (Nadezhina et al., 1987) that is rather common in alkaline rocks (Liferovich and Mitchell, 2006; Chakhmouradian et al., 2002). Slightly increased Si (up to 1.75 wt%) suggests also a limited $Ca^{2+}+P^{5+}$ for $REE^{3+}+Si^{4+}$ (apatite-britholite) substitution (Ito, 1968; Roeder et al., 1987; Pan and Fleet, 2002; Rønsbo, 2008). Maximum concentrations of $(Na,REE)_5(PO_4)_3F$ and $Sr_5(PO_4)_3F$ endmember components corresponded to 40 and 10 mol. %, respectively.

Apatites from syenite correspond to a common fluorapatite with 1.42-2 apfu F, moderate Cl (0-0.26 apfu), nearly constant CaO (55.17-55.67 wt%) and P_2O_5 contents (41.3-42.26 wt%) accompanied by low REE_2O_3 (0.39-1.12 wt%), SrO (0.32-0.35 wt%) and Na_2O contents (below 0.05 wt%). The uniform apatite composition reflects the absence of substitutions on both Ca- and PO_4-sites. Insignificant amounts of FeO and MnO, up to 0.8 and 0.6 wt%, respectively, occurred in all apatites studied.

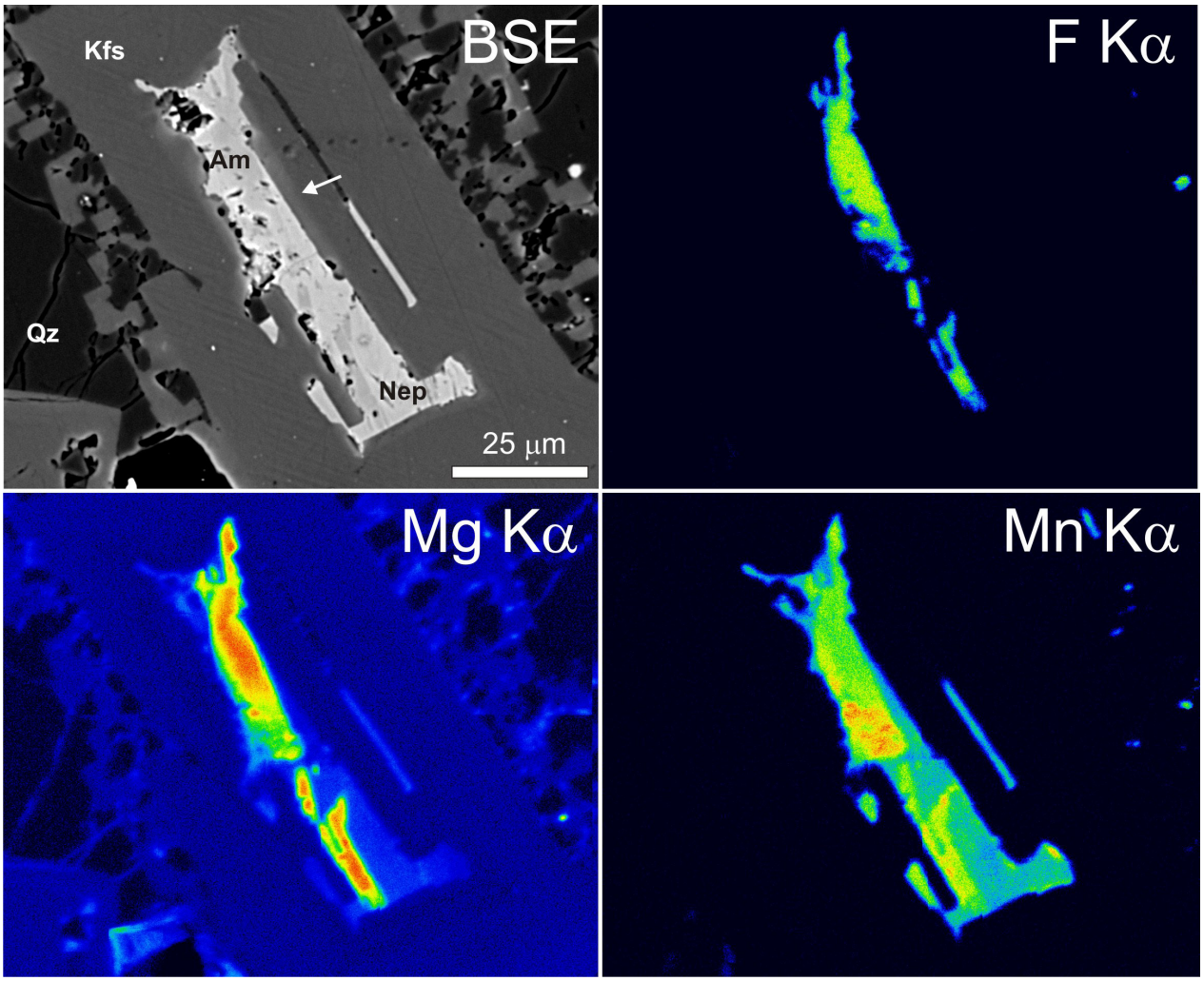

Figure 3. Back-scattered electron image and X-ray maps of "neptunite"-amphibole intergrowth in a hollow in skeletal ferrian feldspar documented in Figure 2a. Mineral abbreviations: Nep-"neptunite", Am-amphibole, Qz-quartz, Kfs-potassium feldspar. Bright arrow indicates Fe-rich zone around central hollow.

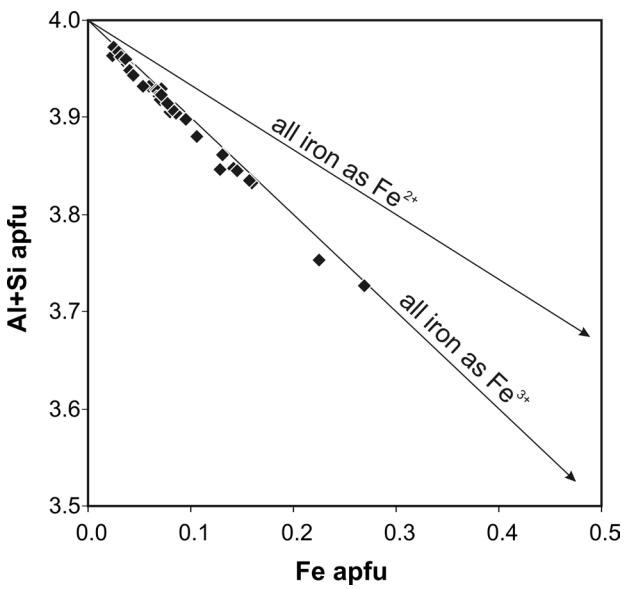

Figure 4. Fe for Al+Si substitution in K-feldspars from Bulhary. Electron probe micro-analyses plot close to the tie-line connecting the $KAlSi_3O_8$ and $KFe^{3+}Si_3O_8$ endmembers, thus showing the absence of divalent iron.

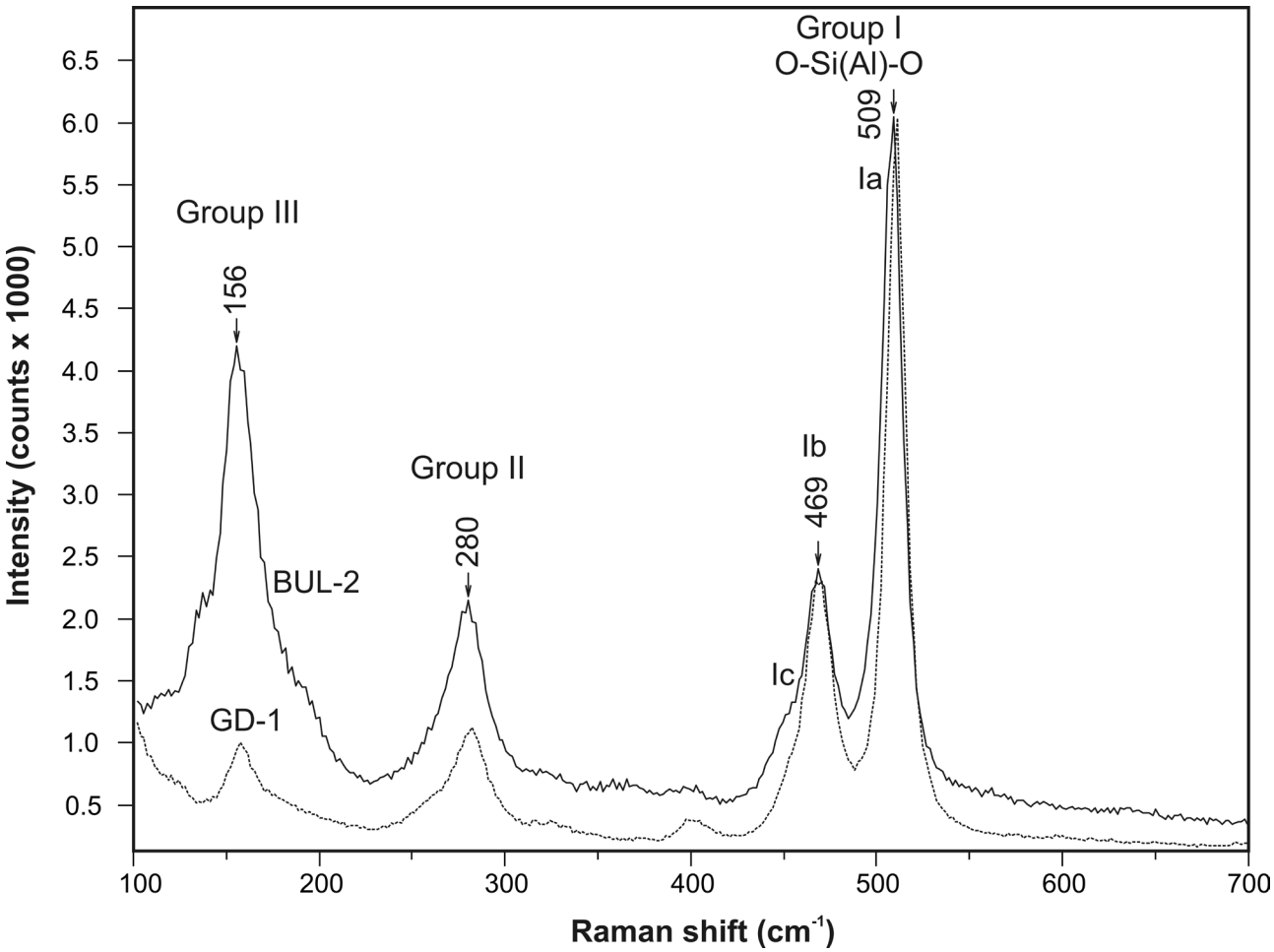

Figure 5. Uncorrected Raman spectra of K-feldspar from Bulhary (BUL-2, solid line) and Na-sanidine ($Or_{53}Ab_{43}$, a=8.390, b=13.009, c=7.166, β=116.11°) megacryst in alkali basalt from Gemerské Dechtáre, southern Slovakia (GD-1, dotted line) recorded using an Xplora Raman spectrometer with 1800 grooves/mm grating, 532 nm excitation, and 2×30 sec. acquisition time. Peak assignments according to Freeman et al. (2008) and Makreski et al. (2009).

Sulphides

Interstitial sulphides correspond mainly to chalcopyrite. Crystallochemical formula - $Cu_{0.88-0.95}Fe_{1.07-1.12}S_2$- recalculated from electron probe micro-analyses (Table S4) indicates the locally moderate sulphur deficiency expressed by the increase in the (Fe+Cu)/S ratio up to 1.03.

Compositions of chalcopyrite-hosted Ni sulphide inclusions (Figure 1 e,f) are similar to that of polydymite/siegenite mineral - $(Ni,Co)_{0.75}S$ (Figure 9, Table S4), albeit with increased Fe and Cu contents. However, electron probe micro-analyses exhibit low totals. Crystallochemical formula normalized to one sulphur atom corresponded to $(Ni_{0.57-0.65}Fe_{0.06-0.12}Cu_{0.06-0.08}Co_{0.02-0.04})_{0.78-0.83}S$.

Cu-sulphide phases around oval Ni-rich inclusions (Figure 1f) and those replacing the chalcopyrite host along cracks and grain boundaries is difficult to identify owing to small dimensions and heterogeneous nature (Figure 1g). Some crack-related Cu-sulphides correspond to bornite ($Cu_{4.73}Fe_{1.15}S_4$). Other, however, plot along the bornite-CuS join (Figure 9). The Cu-richest composition, $Cu_{1.38}Fe_{0.06}S$, projects close to spionkopite ($Cu_{1.39}S$). Cu-sulphide phases precipitating along boundaries of Ni-rich sulphide inclusions (Figure 1f) plot along mixing lines with chalcopyrite or bornite.

Amphiboles

Following recommendations of Oberti et al. (2010) and Hawthorne et al. (2012), as well as substitutional relationships in Ti-rich amphiboles revealed by Leake (1968) and Saxena and Ekström (1970), crystallochemical formulae of amphiboles have been recalculated to 24 (O,OH,F,Cl) atoms, a total of 8 apfu at the T-site (Si, Al, Ti), 2 apfu at the B-site (Ca, Sr, Na), 2 apfu at the W-site (OH,O,F,Cl), and 5 apfu at the C-site (Nb,Ti,Zr,Al,V,

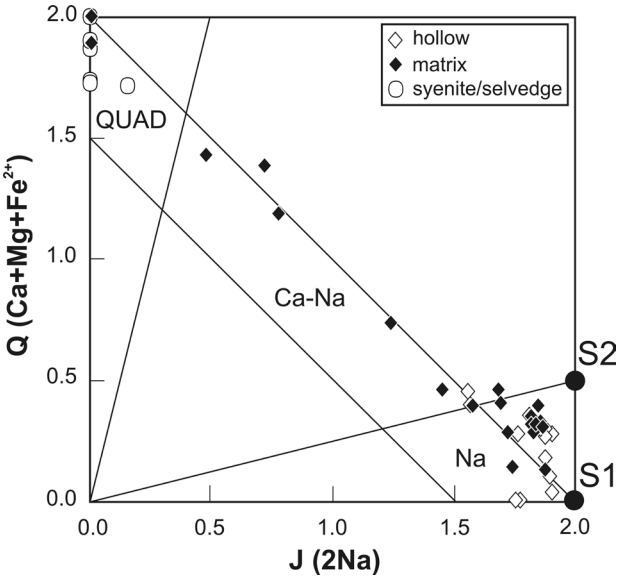

Figure 6. QJ diagram (Morimoto, 1989) for pyroxenes from sample Bul2. Numerous Na-(Ti) pyroxenes from granite matrix and hollows in skeletal K-feldspar project outside the area of "normal" pyroxenes defined by the Q+J=2.0 and Q+J=1.5 lines, owing to the presence of the $NaR^{2+}_{0.5}Ti^{4+}_{0.5}Si_2O_6$ endmember component projected in S2. Shown is also the $NaR^{3+}Si_2O_6$ endmember projected in S1.

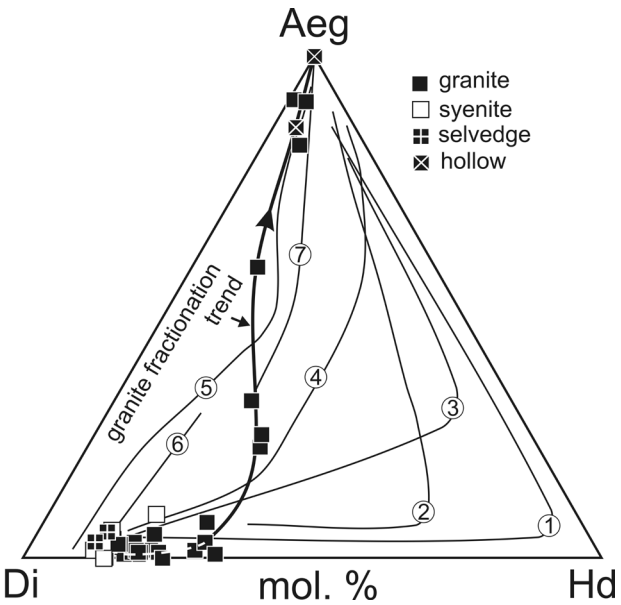

Figure 7. Composition of pyroxenes from Bulhary compared with fractionation trends in alkaline intrusive complexes: 1- Ilímaussaq, Greenland (Larsen, 1976; Marks et al., 2003), 2- Morutu, Japan (Yagi, 1966), 3- Qôroq, Greenland (Stephenson, 1972), 4- Auvergne, France (Varet, 1969), 5- Little Murun, Russia (Mitchell and Vladykin, 1996), 6- Fen, Norway (Mitchell, 1980), 7- Mont Saint-Hilaire, Quebec (Piilonen et al., 1998). Solid curve expresses the fractionation trend of the peralkaline granite from Bulhary. Vectors of other fractionation trends are also oriented towards the aegirine (Aeg) apex. Abbreviations: Di-diopside, Hd-hedenbergite.

Fe^{3+},Fe^{2+},Zn,Mg). OH contents were calculated as equal to $2\text{-}2^{M1}$Ti. Calculations have been made using an Excel spreadsheet (Locock, 2014) extended to incorporate Nb_2O_5. We are aware of the fact that the classification of amphiboles based on electron probe micro-analyses only, with unknown hydroxyl, hydrogen and lithium contents, and oxidation states of iron and manganese may be ambiguous (Hawthorne and Oberti, 2007). Vacancies may also increase the variance of the complex system.

Chemical compositions of matrix and hollow amphiboles (Table S5) exhibit distinct differences. Interstitial amphiboles ranged from obertiite to katophorite, richterite, and arfvedsonite. Incomplete A-site occupancy in these amphiboles may indicate up to 0.2 apfu of vacancies. Worth of noting are increased Nb_2O_5 concentrations, reaching 2.8 wt% (0.18 apfu Nb).

Except for one arfvedsonite analysis (#260), the classification of hollow amphiboles has been always problematic. Owing to their very high titanium content, up to 9 wt% TiO_2, nearly all hollow amphiboles must be classified as oxo-amphiboles with negligible OH contents. Indeed, Raman spectrometric analyses have not revealed any vibrations in the OH-stretching region between 3000 and 4000 cm^{-1}. Provisional recalculations of crystallochemical formulae resulted in cation totals well below the ideal value of 16 and excessive A-site cations counterbalanced by the proportionally deficient C-site. Together with low analytical totals and negligible water concentrations, this would indicate significant amounts of trivalent iron possibly accompanied by lithium. Hence, the analyses have been adjusted to the acceptable amphibole stoichiometry to reach either a total of 5 apfu of C-site cations or the sum of the T+B+C+A cations equivalent to 16 apfu by the Li_2O addition. Theoretical back-calculated lithium contents attained 1.67-1.82 Li_2O (0.96-1.05 apfu Li).

To attain the maximum electroneutrality, iron and manganese in most hollow amphiboles from sample Bul2 must have been considered as trivalent. This resulted in an excess of high-valence cations in the C-site over the maximum value of 2 apfu in "normal" amphiboles (Hawthorne et al., 2012). Hence, the classification scheme based on the amount of C-site cations could not be employed. We have provisionally affiliated the high-valence cation-rich hollow amphiboles from sample Bul2 to ferri-fluoroleakeite. An indirect support for the increased amounts of high-valence cations in the amphiboles is provided by elevated concentrations of the $KFe^{3+}Si_3O_8$ component in adjacent alkali feldspars.

Interstitial amphiboles from other samples match the ideal amphibole stoichiometry without a need for the additional adjustment by surplus Li_2O. $Fe^{3+}/\sum Fe$ ratios calculated from stoichiometry have also been considerably lower, ranging between 0.35 and 0.5, in accord with the depressed Fe^{3+} contents in the associated alkali feldspars.

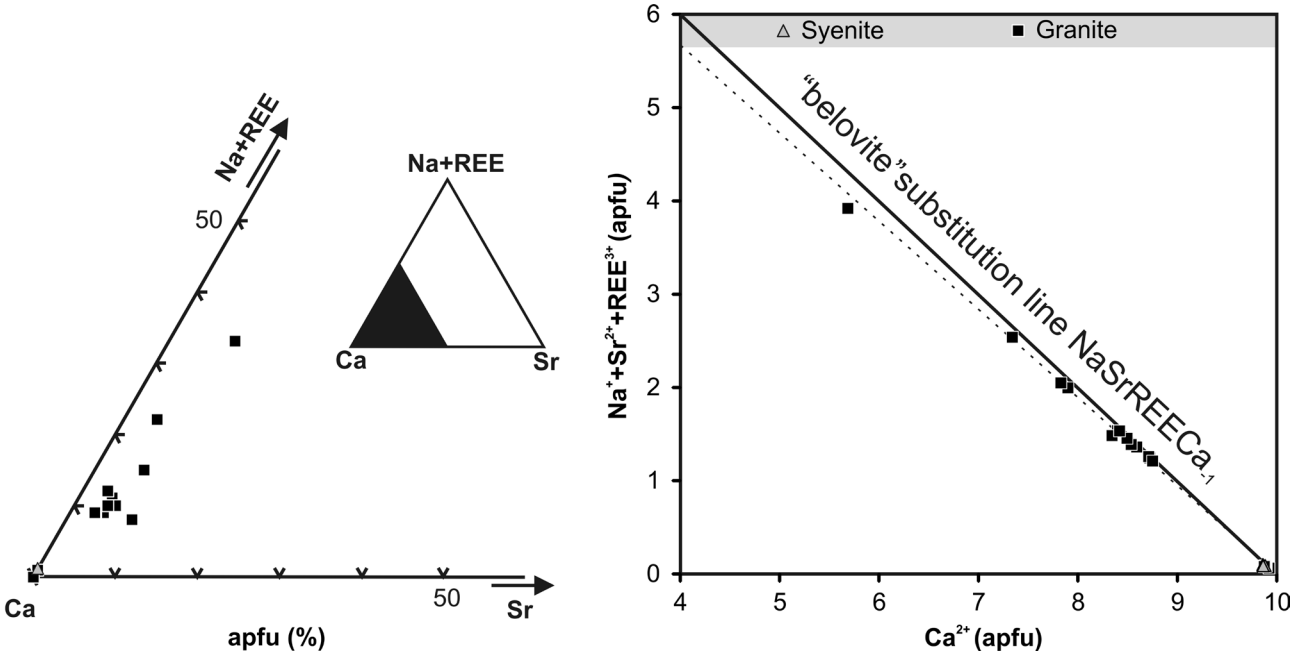

Figure 8. Diagrams showing the NaSrREECa-1 substitution trend in apatites from syenite (n=4) and granite (n=14). Solid and dashed lines represent ideal and observed substitution trends, respectively.

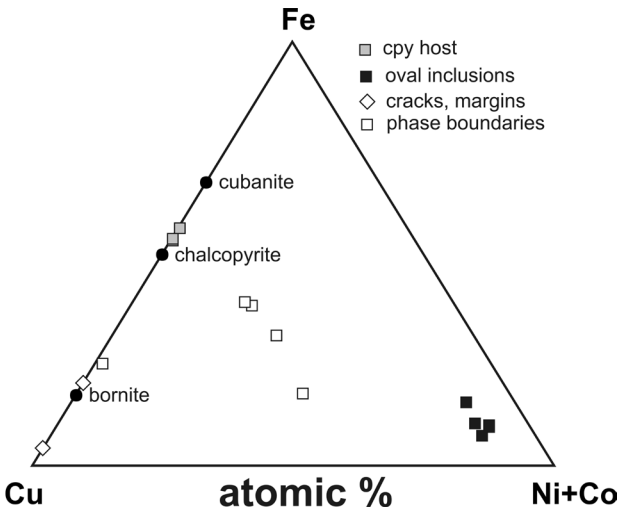

Figure 9. Composition of sulphide phases in granite xenolith Bul7.

Neptunite-like mineral

Some "amphibole" aggregates from hollow feldspar exhibited total cations content close to 15 even if maximum contents of trivalent cations were considered. Moreover, electron probe micro-analyses indicated extreme TiO_2 concentrations, unacceptable for the amphibole-group minerals (Table 3). The unknown mineral was considered neptunite and the chemical analyses have been optimized by the addition of Li_2O until the full cationic charge of 48 or 1 apfu Li, resulting from the ideal neptunite formula -$KNa_2Li(Fe,Mn,Mg)_2Ti_2Si_8O_{24}$, was attained.

Raman spectroscopic study has been performed to corroborate neptunite. However, our spectra differ significantly from published vibrational records of neptunite in the RRUFF spectral database (Lafuente et al., 2015), which all refer to non-magmatic neptunite from San Benito Mountains, California, lacking trivalent cations (Louderback and Blasdale, 1909; Laird and Albee, 1972). Apart from composition, some spectral difference may also result from the directional dependence of the Raman scattering and from high fluorescence excited by 638 nm and 532 nm incident lasers (Figure 10).

The dublet composed of the dominant band at 828-830 cm^{-1} and a smaller satellite band at 868-873 cm^{-1} is the most characteristic identification band of the Bulhary neptunite. A shoulder at ~790 cm^{-1} is recognizable only in certain crystal orientations. The spectrum contrasts with that of the San Benito neptunite, showing only single dominant band, possibly consisting of two components centred at 821-823 and 832 cm^{-1}.

The dominant neptunite band at ~830 cm^{-1} can be attributed to Si-O-Si linkages, whilst the smaller bands between 600 and 800 cm^{-1} can be correlated with Ti-O vibration modes of 4- and 6-coordinated titanium (Colthup et al., 1990; Deo et al., 1993). The band at 790 cm^{-1} is identical with the vibration of the C-site TiO_6 frequently observed in Ti-amphiboles (Leissner et al., 2015). Bands between 600 and 800 cm^{-1} also overlap the Si-O-Si bond symmetric stretching modes in pyroxenes (Wang et al., 1994) and O-Si-O bending modes of the chemically

Table 3. Representative electron probe micro-analyses (wt%) and crystallochemical formulae* of "neptunite"

Sample	Bul2	Bul2	Bul2	Bul2	Bul2	Bul2	Bul2	Bul2	Bul8	Bul8
Anal. #	202	255	257	274	278	302	305	306	401	402
Nb_2O_5	0.47	0.39	0.49	0.56	0.52	1.12	0.84	0.80	<0.15	0.24
SiO_2	50.97	52.98	52.12	50.12	51.56	52.06	51.72	52.15	52.98	52.78
TiO_2	11.10	11.27	9.77	10.26	11.50	12.89	12.06	11.99	16.49	16.39
ZrO_2	0.22	0.21	0.29	0.22	0.24	0.52	0.25	0.29	<0.10	0.09
Al_2O_3	<0.12	0.41	0.15	0.30	0.23	0.16	0.12	0.14	<0.12	<0.12
Fe_2O_3**	13.56	13.01	16.18	16.55	13.88	7.45	12.19	12.35	3.68	3.37
FeO**	1.86	1.00	0.00	0.64	0.74	5.44	1.71	0.00	9.69	9.92
MnO	5.51	5.84	5.79	5.84	7.48	6.46	6.70	7.69	2.46	2.60
ZnO	0.09	<0.09	<0.09	<0.09	<0.09	<0.09	<0.09	<0.09	<0.09	<0.09
MgO	2.20	2.38	2.59	1.22	1.34	1.25	1.59	1.70	1.25	1.08
CaO	0.21	0.18	0.16	0.55	0.22	0.04	0.04	0.03	0.04	0.03
SrO	<0.07	<0.07	na	0.08	<0.07	<0.07	<0.07	<0.07	<0.07	<0.07
BaO	0.80	0.61	0.75	0.65	0.90	0.44	0.31	0.52	0.12	0.32
Li2O	1.43	1.67	1.67	1.62	1.65	1.51	1.64	1.64	1.51	1.51
Na_2O	7.99	7.20	7.41	7.32	7.31	7.14	6.82	6.34	7.15	6.92
K_2O	2.83	3.56	3.46	3.06	3.30	3.64	3.74	3.77	3.52	3.66
F	<0.11	0.18	0.41	<0.11	<0.11	<0.11	<0.11	<0.11	<0.11	<0.11
O=F		-0.08	-0.17							
Σ	*99.24*	*100.82*	*101.07*	*98.99*	*100.87*	*100.12*	*99.74*	*99.41*	*98.89*	*98.91*
Si (apfu)	7.780	7.866	7.773	7.699	7.765	7.890	7.822	7.879	7.983	7.980
Al		0.072	0.026	0.054	0.041	0.029	0.021	0.025		
Ti^{IV}	0.220	0.062	0.201	0.247	0.194	0.081	0.157	0.096	0.017	0.020
ΣT	8.000	8.000	8.000	8.000	8.000	8.000	8.000	8.000	8.000	8.000
Ti^{VI}	1.055	1.197	0.895	0.939	1.109	1.389	1.215	1.267	1.852	1.845
Nb	0.032	0.026	0.033	0.039	0.035	0.077	0.057	0.055		0.016
Zr	0.016	0.015	0.021	0.016	0.018	0.038	0.018	0.021		0.007
Fe^{3+}	1.558	1.454	1.816	1.914	1.573	0.850	1.388	1.404	0.418	0.384
Fe^{2+}	0.237	0.125		0.081	0.093	0.690	0.216		1.220	1.254
Zn	0.010									
Mn	0.712	0.734	0.731	0.760	0.954	0.829	0.858	0.984	0.314	0.333
Mg	0.501	0.527	0.576	0.279	0.301	0.282	0.359	0.383	0.281	0.243
Ca	0.034	0.029	0.026	0.091	0.035	0.006	0.006	0.005	0.006	0.005
Sr				0.007						
Ba	0.048	0.035	0.044	0.039	0.053	0.026	0.018	0.031	0.007	0.019
Li	0.880	1.000	1.000	1.000	1.000	0.921	1.000	0.997	0.915	0.918
Na	2.365	2.073	2.143	2.181	2.135	2.098	1.999	1.858	2.089	2.028
K	0.551	0.674	0.658	0.600	0.634	0.704	0.722	0.727	0.677	0.706
O	2.000	1.915	1.806	2.000	2.000	2.000	2.000	2.000	2.000	2.000
F		0.085	0.194							
Σ *cat.*	*15.999*	*15.889*	*15.943*	*15.947*	*15.940*	*15.910*	*15.855*	*15.732*	*15.778*	*15.758*
Charge+	*48.00*	*47.92*	*47.81*	*48.00*	*48.00*	*48.00*	*48.00*	*48.00*	*48.00*	*48.00*

* recalculated on the basis of 24 O, Li = 1 apfu and/or maximum charge+ = 48
**calculated from stoichiometry assuming maximum electroneutrality
Abbreviations: na- not analyzed

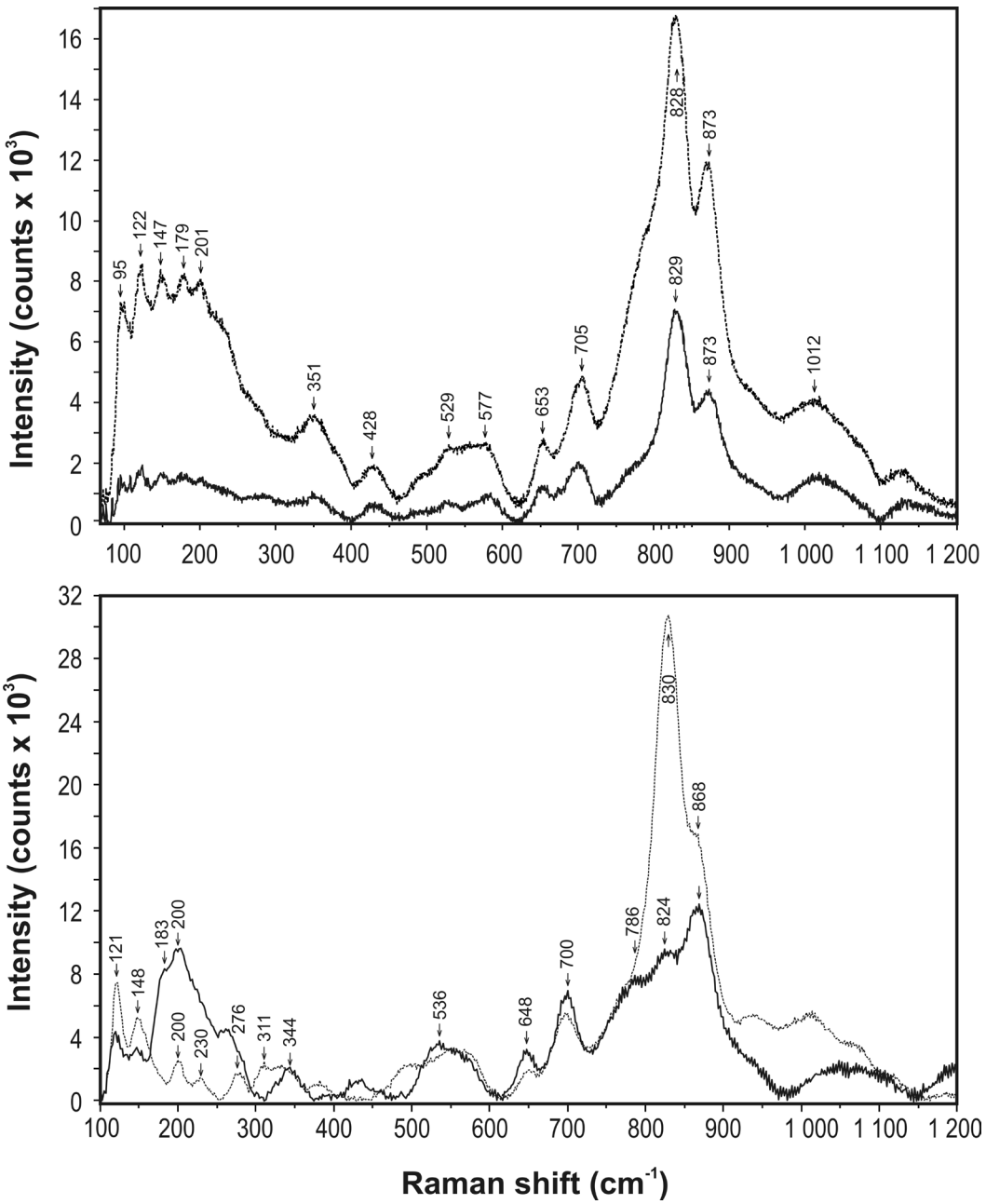

Figure 10. Linear baseline-corrected Raman spectra of neptunite from sample Bul8 (#401, #402) recorded under the following conditions: upper diagram - 1800 grooves/mm grating, 25 % transmission filter, 240 sec. acquisition time, 2 accumulations, 532 nm excitation of a 300 mW Nd-YAG laser of a LabRam800HR system; lower diagram - 1200 grooves/mm grating, no filtering, 40 sec. acquisition time, 2 accumulations, 638 nm excitation of a 18 mW laser of an Xplora system.

similar mineral joaquinite (Frost and Pinto, 2007). The Si-O symmetric stretching vibration region between 990 and 1020 cm^{-1} exhibits only one low intensity band. The lattice vibration region between 100 and 400 cm^{-1} typically exhibits four modes hidden often behind the fluorescence background, whereas bands between 350 and 450 cm^{-1} can be attributed to Fe-O and Mg-O bonds of octahedral cations similar to those in amphiboles (Apopei et al., 2011).

Dominant 830 and 865-875 cm^{-1} bands allow for "neptunite" diagnostics in fluorescent crystal aggregates, as it is documented by the Raman mapping (Figure 11). Apart from the "neptunite", the mapping of hollow assemblage confirmed apatite and also revealed an unidentified transparent phosphate with sharp vibration bands at 488, 540, 936 and 956 cm^{-1}.

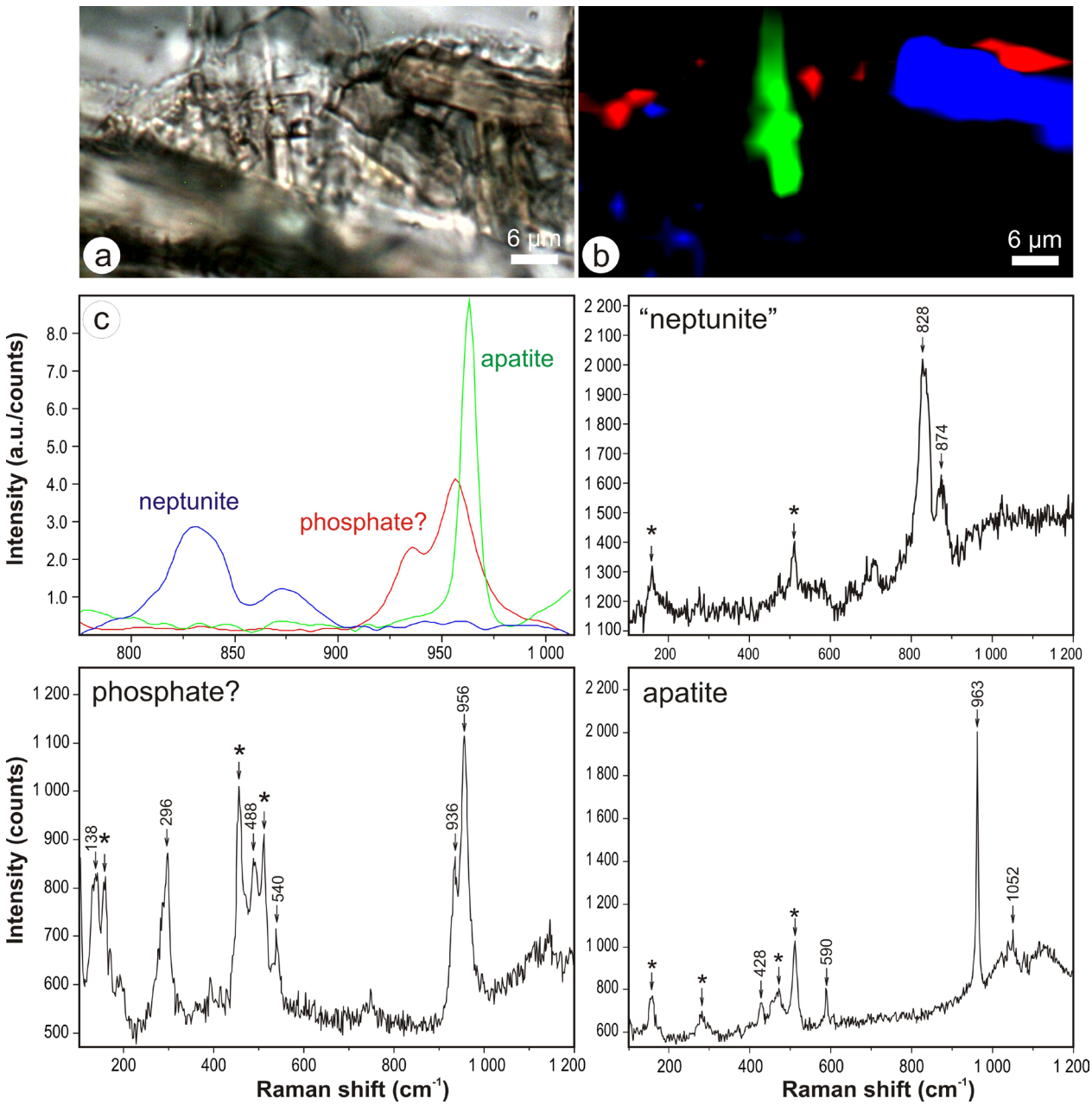

Figure 11. Raman mapping of a hollow in sample Bul2. a) Magnified view of the rectangle in Figure 2b showing brown neptunite crystals and numerous transparent minerals. b) Raman map of the previous image in false colors produced by the factor analysis algorithm included in the Labspec5 software from Horiba Ltd., Japan. The factor analysis based on smoothed, background-corrected reference spectra in c) revealed neptunite (blue), apatite (green) and an unknown transparent mineral (red) - probably another phosphate. Other diagrams show uncorrected Raman spectra of these minerals obtained using the 532 nm excitation, 2×7 sec. acquisition time of the LabramHR800 spectrometer from Horiba Ltd., Japan. Bands denoted by asterisks belong to the feldspar host.

DISCUSSION

Crystallization conditions and parental magma

Granite-syenite nodules from the Bulhary open pit are unusual by an increased amount of Zr, Nb and Ti in coexisting clinopyroxenes and amphiboles. The incorporation of Zr and Nb in the rock-forming silicates is a consequence of melt depolymerization by alkalis accompanied by the stabilization of [6]-coordinated Zr, which fits into the M1 structural sites of chain silicates (Farges et al., 1994; Piilonen et al., 1998).

The investigated xenoliths are further exceptional due to their anhydrous character and oxidizing

crystallization conditions buffered by hematite. As a consequence, increased ferric iron contents occur in late mineral assemblages preserved in K-feldspar hollows. Combination of excessive Fe^{3+} combined with the strong depletion in alumina of the parental magma recorded in primary silicate melt inclusions in pyroxenes resulted in the crystallization of ferrian sanidine-anorthoclase, in which the Al deficit was compensated by ferric iron. The skeletal morphology and the specific fractal growth of the anorthoclase-sanidine aggregates associated with quartz suggest near-solidus crystallization from a supersaturated melt due to loss of volatiles (e.g., Smith and Franks, 1986). Peralkaline character of granite-syenite nodules from Bulhary is underlined by Na-Sr-REE-rich apatite, Na-REE-rich titanite, alkali amphiboles, and aegirine in granite, and sodalite and nepheline in syenite.

High ferric iron contents in sanidine-anorthoclase from Bulhary is an important genetic indicator and rarely observed phenomenon. Ferrian sanidine is common in lamproites, where the highest ferric iron contents, up to 18.4 wt% Fe_2O_3, has been recorded (Linthout and Lustenhouwer, 1993; Kuehner and Joswiak, 1996). Considering the strong Al deficit and enrichment in Fe^{3+}, the granite from Bulhary has features reminiscent of lamproites and lamprophyres, albeit with a low magnesium content. Such granites may be derived from the lamprophyric magma by fractional crystallization of diopside.

The mafic parental magma of alkali granites from Bulhary is indirectly documented by interstitial Cu-Ni-(Co) sulphides, which show textural signs of immiscible separation of Ni-rich sulphide melt by liquation (Figure 1 e,f). Disseminated Cu-Ni-(PGE-Au) mineralization represented by blebby accumulations of chalcopyrite, pyrite, millerite, bravoite, hengleinite, violarite and gersdorffite rarely occurs in alkaline granodiorites and granites of the appinite suite genetically related to the fractional crystallization from lamprophyric magma and crystal accumulation of amphiboles (Barnes et al., 2008; Graham et al., 2017).

Age of peralkaline nodules from Bulhary remains unknown. Lacking metamorphic overprint, hydrothermal alteration, and tectonic modification indicate their affiliation with other Pliocene intra-plate anorogenic granites of the Carpathian back-arc basin. If true, then peralkaline nodules from Bulhary extends the compositional variability of the A-type granitoid xenoliths hitherto described from Pliocene-Pleistocene alkali basalts of Western Carpathians: a 5.4 Ma old, magnesian, calcian, peraluminous, orthopyroxene granite (pincinite) from the Pinciná maar near Lučenec (Huraiová et al., 1996, 2005; Hurai et al., 2010), and a 5.2 Ma old, ferroan, calc-alkaline, peraluminous granite from the basaltic lava flow near Čamovce village (Huraiová et al., 2015).

Composition and origin of neptunite-like mineral

The discovery of neptunite-like mineral in peralkaline granites from Bulhary supplements other occurrences of neptunite in peralkaline and hyper-alkaline (agpaitic) syenites, pegmatites and their fenite aureoles (e.g., Flink, 1893; Bøggild, 1905; Fersman, 1926; Nockolds, 1950; Heinrich and Quon, 1963; Dusmatov and Kabanova, 1967; Birkett et al., 1996; Chakmouradian and Mitchell, 2002; Petersen and Johnsen, 2005; Yakovenchuk et al., 2007; Vilalva et al., 2016).

Calculated ferric iron contents in "neptunites" from Bulhary, particularly in sample Bul2, were extraordinary high. In some analyses, not only the ferric iron content exceeds nearly twice that of the octahedrally coordinated titanium, but it also overwhelms divalent cations, even if all Mn is considered as divalent. $Fe^{3+}/\sum Fe$ ratios recalculated from ideal neptunite stoichiometry and the maximal electroneutrality corresponded to 0.7-1 in granite Bul2 and to around 0.4 in granite Bul8, thus reflecting different oxidation degrees mirrored in Fe^{3+} contents of the associated feldspars and amphiboles. The ferric iron content in our "neptunites" was inversely correlated with that of Ti, thus indicating the Fe^{3+}-for-Ti^{4+} substitution compensated partly by up to 0.08 apfu Nb^{5+}. The provisional crystallochemical formula of the neptunite-like mineral from strongly oxidized sample Bul2 corresponds to

$$\square_{0.08\text{-}0.28}(Na,K)_{0.72\text{-}0.92}Na_{1.86\text{-}2}Li_{0.88\text{-}1}(Mn,Mg,Fe)_{1.12\text{-}1.8}(Fe^{3+})_{0.85\text{-}1}(Ti,Fe^{3+})_{1.39\text{-}1.85}(Si,Ti)_8O_{23}(O,F).$$

Particularly noticeable are totals of alkalis (Na+K+Li) below the ideal value of 4 apfu, high calculated ferric iron contents and Ti contents less than 2 apfu, possibly indicating hypothetical ferri-neptunite endmember $-\square(M^+)_2Li(Mn,Fe^{3+})_3TiSi_8O_{24}$.

It is possible that neptunite-like minerals from Bulhary could accommodate up to 0.2 apfu of fluorine in their structure, as it has already been documented for neptunite in other localities. This behaviour has been observed in the Strange Lake peralkaline granite complex of Quebec, Labrador, Canada (Birkett et al., 1996), where Fe^{3+}-bearing neptunite coexisted with Li-bearing arfvedsonite (Hawthorne et al., 2001). In Bulhary, alkali amphiboles intergrown with "neptunite" have been tentatively classified as leakeite, assuming 0.96-1.05 apfu Li back-calculated from stoichiometry. However, amounts of trivalent cations and lithium may have been overestimated, as it had also been documented in the Strange Lake amphiboles, where direct determinations proven only up to 0.4 apfu Li, and less than 2 apfu Fe^{3+} (Hawthorne et al., 2001).

Neptunite is often attributed to the hydrothermal alteration of Ti-bearing minerals (Flink, 1893; Nockolds, 1950; Bondam and Sørensen, 1959; Marks et al., 2004), metabasalts, blueschists and amphibolite schists

(Louderback and Blasdale, 1909; Laird and Albee, 1972), granulite xenoliths in agpaitic syenite intrusions (Arzamastsev et al., 2000), and amphiboles in peralkaline and hyper-alkaline (agpaitic) felsic igneous rocks (Vilalva et al., 2016). In contrast, magmatic conditions in excess of 800 °C have been proposed for the crystallization of neptunite associated with sanidine and silicate glass in skarnified (fenitized) carbonate, siltstone and sandstone xenoliths entrained in rhyolitic and rhyodacitic ignimbrites (Zadov et al., 2011).

In Bulhary, titanian aegirine, "neptunite" and Li-amphiboles cannot be associated with the hydrothermal alteration by pervasive fluids, because they only occur in feldspar hollows. On the other hand, the drusy appearance of the assemblage is reminiscent of the crystallization from a fluid rather than melt. Hence, "neptunite" together with associated minerals can be provisionally attributed to a late-magmatic crystallization from volatile melt close to the granite solidus.

CONCLUSIONS

We describe the first occurrence of peralkaline igneous rocks in Western Carpathians. The investigated xenoliths entrained in Pleistocene alkali basalt are composed of alkali amphibole-bearing peralkaline, metaluminous granite enclosed in nepheline-sodalite syenite. The granite nodules from Bulhary provide evidence for a well-differentiated crustal magmatic reservoir, producing the variegated inventory of felsic magmatic rocks by the fractionational crystallization of mantle-derived mafic magmas modified by interactions with the lower crust and/or the metasomatized upper mantle.

ACKNOWLEDGEMENTS

Early draft of the manuscript benefited from critical comments of two anonymous reviewers. The laboratory of vibrational spectroscopy at the Institute of Earth Sciences, Slovak Academy of Sciences, was established due to financial support from the European Regional Development Fund under the project of the Centre of Excellence for Integrated Research of the Earth´s Geosphere (ITMS-26220120064).

REFERENCES

Apopei A.I., Buzgar N., Buzatu A., 2011. Raman and infrared spectroscopy of kaersutite and certain common amphiboles. Analele Stiintifice ale Universitatii Ai. I. Cuza din Iasi Seria Geologie 57, 35-58.

Arzamastsev A.A., Belyatsky B.V., Arzamastseva L.V., 2000. Agpaitic magmatism in the northeastern Baltic Shield: a study of the Niva intrusion, Kola Peninsula, Russia. Lithos 51, 27-46.

Barnes S.J., Anderson J.A.C., Smith T.R., Bagas L., 2008. The Mordor Alkaline Igneous Complex, Central Australia: PGE-enriched disseminated sulfide layers in cumulates from a lamprophyric magma. Mineralium Deposita 43, 641-662.

Birkett T.C., Trzcienski W.E.Jr., Stirling J.A.R., 1996. Occurrence and compositions of some Ti-bearing minerals in the Strange Lake intrusive complex, Quebec-Labrador boundary. Canadian Mineralogist 34, 779-801.

Bondam J. and Sørensen H., 1959. Uraniferous nepheline syenites and related rocks in the Ilímaussaq area, Julianehaab District, southwest Greenland. Proceedings of the 2nd UN Geneva Conference on the Peaceful Uses of Atomic Energy 2, 555-559.

Bøggild O.B., 1905. Mineralogia Groenlandica. Meddelelser Om Grønland 32, 502-506.

Colthup N.B., Daly L.H., Wiberley S.E., 1990. Introduction to Infrared and Raman Spectroscopy, 3rd Edition. Academic Press, San Diego, London, 547 pp.

Deo G., Turek A.M., Wachs I.E., Huybrechts D.R.C., Jacobs P.A., 1993. Characterization of titania silicates. Zeolites 13, 365-373.

Dobosi G., Fodor R.V., Goldberg S.A., 1995. Late-Cenozoic alkali basalt magmatism in Northern Hungary and Slovakia: petrology, source compositions and relationships to tectonics. Acta Vulcanologica 7, 189-198.

Downes H., Pantó Gy., Póka T., Mattey D.P., Greenwood P.B., 1995. Calc-alkaline volcanics of the Inner Carpathian arc, Northern Hungary: new geochemical and oxygen isotopic results. Acta Vulcanologica 7, 29-41.

Dusmatov V.D. and Kabanova L.K., 1967. Finding of neptunite in Tadjikistan. Doklady AN TadzhSSR 10, 40-42.

Farges F., Brown G.E., Velde D., 1994. Structural environment of Zr in two inosilicates from Cameroon: mineralogical and geochemical implications. American Mineralogist 79, 838-847.

Fersman A.E., 1926. Minerals of the Kola Peninsula. American Mineralogist 11, 289-299.

Flink G., 1893. Om några mineral från Grönland. Geologiska Föreningens Förhandlingar 151, 195-208.

Freeman J.J., Wang A., Kuebler K.E., Jolliff B.L., Haskin L.A., 2008. Characterization of natural feldspars by Raman spectroscopy for future planetary exploration. Canadian Mineralogist 46, 1477-1500.

Frost R.L. and Pinto C., 2007. Raman spectroscopy of the joaquinite minerals. Journal of Raman Spectroscopy 38, 841-845.

Graham S.D., Holwell D.A., McDonald I., Jenkin G.R.T., Hill N.J., Boyce A.J., Smith J., Sangster C., 2017. Magmatic Cu-Ni-PGE-Au sulfide mineralisation in alkaline igneous systems: An example from the Sron Garbh intrusion, Tyndrum, Scotland. Ore Geology Reviews 80, 961-984.

Hawthorne F.C. and Oberti R., 2007. Amphiboles: Crystal chemistry. Reviews in Mineralogy and Geochemistry 67, 1-54.

Hawthorne F.C., Oberti R., Cannillo E., Ottolini L., 2001. Li-bearing arfvedsonitic amphiboles from the Strange Lake peralkaline granite, Quebec. Canadian Mineralogist 39, 1161-1170.

Hawthorne F.C., Oberti R., Harlow G.E., Maresch W.V., Martin R.F., Schumacher J.C., Welch M.D., 2012. Nomenclature of the amphibole supergroup. American Mineralogist 97, 2031-2048.

Heinrich E.W. and Quon S.H., 1963. Neptunite from Seal Lake, Labrador. Canadian Mineralogist 7, 650-654.

Hurai V., Paquette J.-L., Huraiová M., Konečný P., 2010. U-Th-Pb geochronology of zircon and monazite from syenite and pincinite xenoliths in Pliocene alkali basalts of the intra-Carpathian back-arc basin. Journal of Volcanology and Geothermal Research 198, 275-287.

Huraiová M., Konečný P., Konečný V., Simon K., Hurai V., 1996. Mafic and salic igneous xenoliths in Late Tertiary alkaline basalts: Fluid inclusion and mineralogical evidence for a deep-crustal magmatic reservoir in the Western Carpathians. European Journal of Mineralogy 8, 901-916.

Huraiová M., Dubessy J., Konečný P., Simon K., Kráľ J., Zielinski G., Lipka J., Hurai V., 2005. Glassy orthopyroxene granodiorites of the Pannonian Basin: tracers of ultra-high-temperature deep-crustal anatexis triggered by Tertiary basaltic volcanism. Contributions to Mineralogy and Petrology 148, 615-633.

Huraiová M., Hurai V., Paquette J.-L., 2015. Petrogenesis of Miocene-Pliocene A-type granitoids of southern Slovakia. Acta Geologica Slovaca 7, 37-50 (in Slovak).

Chakhmouradian A.R. and Mitchell R.H., 2002. The mineralogy of Ba- and Zr-rich alkaline pegmatites from Gordon Butte, Crazy Mountains (Montana, USA), comparisons between potassic and sodic agpaitic pegmatites. Contributions to Mineralogy and Petrology 143, 93-114.

Chakhmouradian A.R., Reguir E.P., Mitchell R.H., 2002. Strontium apatite: New occurrences, and the extent of Sr-for-Ca substitution in apatite-group minerals. Canadian Mineralogist 40, 121-136.

Ito J., 1968. Silicate apatites and oxyapatites. American Mineralogist 53, 890-907.

Konečný V. and Lexa J., 2003. Evolution of the phreatomagmatic/extrusive/intrusive complex of the Bulhary maar-diatreme volcano in southern Slovakia. Geolines 15, 47-51.

Konečný V., Lexa J., Balogh K., Konečný P., 1995. Alkali basalt volcanism in Southern Slovakia: volcanic forms and time evolution. Acta Vulcanologica 7, 167-172.

Konečný V., Kováč M., Lexa J., Šefara J., 2002. Neogene evolution of the Carpatho-Pannonian region: an interplay of subduction and back-arc diapiric uprise in the mantle. EGS Stephan Mueller Special Publication Series 1, 165-194.

Konečný V., Balogh K., Orlický O., Vass D., Lexa J., 2003. Timing of the Neogene-Quaternary alkali basalt volcanism in Central and Southern Slovakia (Western Carpathians). Geologica Carpathica 53, Special Issue, Proceedings of the XVIIth Congress of the Carpathian-Balkan Geological Association, Bratislava, September 1-4, 2002, CD version, ISSN 1335-0552.

Kroll H. and Ribbe P.H., 1983. Lattice parameters, composition, and Al/Si order in alkali feldspars. Reviews in Mineralogy and Geochemistry 2, 57-99.

Kuehner S.M. and Joswiak D.J., 1996. Naturally occurring ferric iron sanidine from the Leucite Hills lamproite. American Mineralogist 81, 229-237.

Lafuente B., Downs R.T., Yang H., Stone N., 2015. The power of databases: the RRUFF project. In: Highlights in Mineralogical Crystallography. (eds): T. Armbruster and R.M. Danisi, W. De Gruyter, Berlin, 1-30.

Laird J. and Albee A.L., 1972. Chemical composition and physical, optical, and structural properties of benitoite, neptunite and joaquinite. American Mineralogist 57, 85-102.

Larsen L.M., 1976. Clinopyroxenes and coexisting mafic minerals from the alkaline Ilímaussaq intrusion, south Greenland. Journal of Petrology 17, 258-290.

Leake B.E., 1968. A catalog of analyzed calciferous and subcalciferous amphiboles together with their nomenclature and associated minerals. Geological Society of America Special Paper, 98.

Leissner L., Schlüter J., Horn I., Mihailova B. 2015. Exploring the potential of Raman spectroscopy for crystallochemical analyses of complex hydrous silicates: I. Amphiboles. American Mineralogist 100, 2682-2694.

Liferovich R.P. and Mitchell R.H., 2006. Apatite-group minerals from nepheline syenite, Pilansberg alkaline complex, South Africa. Mineralogical Magazine 70, 463-484.

Linthout K. and Lustenhouwer W.J., 1993. Ferrian high sanidine in a lamproite from Cancarix, Spain. Mineralogical Magazine 57, 289-299.

Locock A.J., 2014. An Excel spreadsheet to classify chemical analyses of amphiboles following the IMA 2012 recommendations. Computers and Geosciences 62, 1-11.

Louderback G.D. and Blasdale W.C., 1909. Benitoite, its paragenesis and mode of occurrence. University of California Department Geology Bulletin 5, 331-380.

Makreski P., Jovanovski G., Kaitner B., 2009. Minerals from Macedonia. XXIV. Spectra-structure characterization of tectosilicates. Journal of Molecular Structure 924-926, 413-419.

Marks M., Vennemann T., Siebel W., Markl G., 2003. Quantification of magmatic and hydrothermal processes in a peralkaline syenite-granite complex based on textures, phase equilibria, and stable and radiogenic isotopes. Journal of Petrology 44, 1247-1280.

Marks M., Halama R., Wenzel T., Markl G., 2004. Trace element variations in clinopyroxene and amphibole from alkaline to peralkaline syenites and granites: implications for mineral-melt trace-element partitioning. Chemical Geology 211, 185-215.

Mitchell R.H., 1980. Pyroxenes of the Fen alkaline complex, Norway. American Mineralogist 65, 45-54.

Mitchell R.H. and Vladykin N.V., 1996. Compositional variation of pyroxene and mica from the Little Murun ultrapotassic complex, Aldan Shield, Russia. Mineralogical Magazine 60, 907-925.

Morimoto N., Fabries J., Ferguson A.K., Ginzburg I.V., Ross M., Seifert F.A., Zussman J., Aoki K., Gottardi G., 1989. Nomenclature of pyroxenes. Canadian Mineralogist 27, 143-156.

Nadezhina T.N., Pushcharovsky D.Yu., Khomyakov A.P., 1987. Refinement of crystal structure of belovite. Mineralogicheskiy Zhurnal 9, 45-48 (in Russian).

Nockolds S.R., 1950. On the occurrence of neptunite and eudialyte in quartz-bearing syenites from Barnavave, Carlingford, Ireland. Mineralogical Magazine 29, 27-33.

Oberti R., Boiocchi M., Hawthorne F.C., Robinson P., 2010. Crystal structure and crystal chemistry of fluoro-potassic-magnesio-arfvedsonite from Monte Metocha, Xixano region, Mozambique, and discussion of the holotype from Quebec, Canada. Mineralogical Magazine 74, 951-960.

Pan Yu. and Fleet M., 2002. Compositions of apatite-group minerals: substitution mechanism and controlling factors.

In: Phosphates - Geochemical, Geological, and Materials Importance. (eds): M.J. Kohn, J. Rakovan, J.M. Hughes, Reviews in Mineralogy and Geochemistry 38. Mineralogical Society of America and the Geochemical Society, Washington, D.C., 13-49.

Papike J.J., Cameron K.L., Baldwin K., 1974. Amphiboles and pyroxenes: characterization of other than quadrilateral components and estimates of ferric iron from microprobe data. Geological Society of America, Abstract with Programs 6, 1053-1054.

Pasero M., Kampf A.R., Ferraris C., Pekov I.V., Rakovan J., White T.J., 2010. Nomenclature of the apatite supergroup minerals. European Journal of Mineralogy 22, 163-179.

Pécskay Z., Lexa J., Szakács A., Seghedi I., Balogh K., Konečný V., Zelenka T., Kovacs M., Póka T., Fülöp A., Márton E., Panaiotu C., Cvetković V., 2006. Geochronology of Neogene magmatism in the Carpathian arc and intra-Carpathian area. Geologica Carpathica 57, 511-530.

Petersen O.V. and Johnsen O., 2005. Mineral species first described from Greenland. Canadian Mineralogist Special Publication 8, 76-77.

Piilonen P.C., McDonald A.M., Lalonde A.E., 1998. The crystal chemistry of aegirine from Mont Saint-Hilaire, Quebec. Canadian Mineralogist 36, 779-791.

Pouchou J.L. and Pichoir F., 1984. Un nouveau modèle de calcul pour la microanalyse quantitative par spectrométrie de rayons X - Partie II : application à l'analyse d'échantillons hétérogènes en profondeur. Recherché Aerospatiale 5, 349-367.

Roeder P.L., MacArthur D., Ma X.-P., Palmer G.R., Mariano A.N., 1987. Cathodoluminescence and microprobe study of rare-earth elements in apatite. American Mineralogist 72, 801-811.

Rønsbo J.G., 2008. Apatite in the Ilímaussaq alkaline complex: Occurrence, zonation and compositional variation. Lithos 106, 71-82.

Ryburn R., Råheim A., Green D.H., 1976. Determination of the P,T paths of natural eclogites during metamorphism-record of subduction: A correction to a paper of Råheim and Green, 1975). Lithos 9, 161-164.

Saxena S.K. and Ekström, T.K., 1970. Statistical chemistry of calcic amphiboles. Contributions to Mineralogy and Petrology 26, 276-284.

Seghedi I., Downes H., Vaselli O., Szakács A., Balogh K., Pécskay Z., 2004. Postcollisional Tertiary-Quaternary mafic alkalic magmatism in the Carpathian-Pannonian region: a review. Tectonophysics 393, 43-62.

Seifert W., Kampf H., Wasternack J., 2000. Compositional variation in apatite, phlogopite and other accessory minerals of the ultramafic Delitzsch complex, Germany: implication for cooling history of carbonatites. Lithos 53, 81-100.

Smith M.P. and Franks P.C., 1986. Mg-rich hollow sanidine in partially melted granite xenoliths in a mica peridotite at Rose dome, Woodson County, Kansas. American Mineralogist 71, 60-67.

Stephenson D., 1972. Alkali clinopyroxenes from the nepheline syenites of the south Qôroq centre, south Greenland. Lithos 5, 187-201.

Varet J., 1969. Les pyroxènes des phonolites du Cantal (Auvergne, France). Neues Jahrbuch für Mineralogie Monatshefte, 174-185.

Vilalva F.C.J., Vlach S.R.F., Simonetti A., 2016. Chemical and O-isotope compositions of amphiboles and clinopyroxenes from A-type granites of the Papanduva Pluton, south Brazil: Insights into late- to post-magmatic evolution of peralkaline systems. Chemical Geology 420, 186-199.

Wang A., Han J., Guo J.Y., Zeng P., 1994. Database of standard Raman spectra of minerals and related inorganic crystals. Applied Spectroscopy 48, 959-968.

Yagi K., 1966. The system acmite-diopside and its bearing on the stability relations on natural pyroxenes of the acmite - hedenbergite - diopside series. American Mineralogist 51, 976-1000.

Yakovenchuk V.N., Krivovichev S.V., Pakhomovsky Y.A., Ivanyuk G.Yu., Selivanova E.A., Men´shikov Yu.P., Britvin S.N., 2007. Armbrusterite, $K_5Na_6Mn_3+Mn_2+14[Si_9O_{22}]4.4H_2O$, a new Mn hydrous heterophyllosilicate from the Khibiny alkaline massif, Kola Peninsula, Russia. American Mineralogist 92, 416-423.

Yavuz F., 2013. WinPyrox: A Windows program for pyroxene calculation, classification and thermobarometry. American Mineralogist 98, 1338-1359.

Zadov A.E., Gazeev V.M., Karimova O.V., Pertsev N.N., Pekov I.V., Galuskin E.V., Galuskina I.O., Gurbanov A.G., Belakovsky D.I., Borisovsky S.E., Kartashov P.M., Ivanova A.G., Yakubovich O.V., 2011. Magnesioneptunite, $KNa_2Li(Mg, Fe)_2Ti_2Si_8O_{24}$, a new mineral species of the neptunite group. Geology of Ore Deposits 53, 775-782.